Petroleum Science 23 (2026) 7472–7486

Contents lists available at ScienceDirect

Petroleum Science

journal homepage: www.keaipublishing.com/en/journals/petroleum-science

Original Paper

Waste-derived ZnO nanoparticles with dual electrochemical-microbial inhibition functions: A green strategy for petroleum pipeline corrosion control

Fu-Li Wu [a,1], Qi-You Liu [a,b,*,1], Yu-Hua Su [a], Guang-Lei Lv [c], Peng Xiao [a], Lei Lu [a,b], Yong-Qiang Wang [a,b], Gang Wang [a,b]

[a] College of Chemistry and Chemical Engineering, China University of Petroleum (East China), Qingdao, 266580, Shandong, China
[b] State Key Laboratory of Heavy Oil Processing, China University of Petroleum (East China), Qingdao, 266580, Shandong, China
[c] CNOOC (Tianjin) Pipeline Engineering Technology Ltd., Tianjin, 300452, China

ARTICLE INFO

Article history:
Received 25 May 2025
Received in revised form
17 March 2026
Accepted 23 June 2026
Available online 4 July 2026

Edited by Xi Zhang

Keywords:
Corrosion inhibition
Electrochemical impedance spectroscopy
Green synthesis
Sulfate-reducing bacteria
Zinc oxide nanoparticles

ABSTRACT

Microbiologically influenced corrosion (MIC), primarily caused by sulfate-reducing bacteria (SRB) biofilms, presents a significant challenge to the integrity of petroleum pipeline systems. In this study, zinc oxide nanoparticles (ZnO NPs) were green-synthesized using tomato peel extract and evaluated for their corrosion inhibition performance in anaerobic conditions. The presence of phytochemicals in the extract facilitated the formation of hexagonal wurtzite-structured ZnO NPs (with a size range of 20–45 nm) with organic-inorganic hybrid interfaces, enhancing their interfacial interaction and anti-biofilm capability. Surface-bound biomolecules rapidly adsorbed onto the metal surface, forming a transient passivation layer that effectively suppressed early-stage corrosion by retarding initial anodic dissolution. The green-synthesized ZnO NPs achieved a 90.6% reduction in viable SRB cells, reduced corrosion rate by 74.2% (based on weight loss), decreased corrosion pit depth by 83.9% (via 3D profilometry), and inhibited biofilm formation by 67.5% (quantified by CLSM). Electrochemical impedance spectroscopy further showed that the green ZnO NPs increased charge-transfer resistance by approximately 13 times and 11 times after 7 and 28 days, respectively, outperforming chemically synthesized ZnO NPs by about 7.8 times. The enhanced electrochemical performance, combined with the sustainable origin derived from agricultural waste and the environmental friendliness of the synthesis process, underscores the potential of tomato peel-derived ZnO NPs as an efficient and eco-friendly alternative for MIC mitigation in oilfield pipeline systems.

© 2026 The Authors. Publishing services by Elsevier B.V. on behalf of KeAi Communications Co. Ltd. This is an open access article under the CC BY-NC-ND license (http://creativecommons.org/licenses/by-nc-nd/4.0/).

1. Introduction

As core infrastructure for global energy transportation, the safety and durability of oil pipelines directly affect energy supply stability. The long-term anaerobic and humid environment inside pipelines provides ideal conditions for corrosive microorganisms such as sulfate-reducing bacteria (SRB) and acid-producing bacteria (APB) (Pereira et al., 2024). SRB metabolize sulfate to produce hydrogen sulfide (H_2S), which reacts with metal surfaces to generate FeS corrosion products and induces localized acidification, accelerating pitting corrosion and stress corrosion cracking (Xing et al., 2025; Yang et al., 2020). Microbial corrosion (MIC) causes annual losses exceeding $1 billion in the global oil industry (Jia et al., 2019), making the development of efficient and sustainable MIC inhibition technologies a critical issue in the energy sector.

Conventional biocides (e.g., quaternary ammonium salts, nitrates) can inhibit microbial activity in the short term, but their long-term use may induce drug resistance and pose ecological risks due to high toxicity (Lv et al., 2024; Nguyen et al., 2012). Physical protection techniques (e.g., coatings, cathodic protection) are often insufficiently stable under complex conditions to counter

* Corresponding author.
E-mail address: liuqiyou@upc.edu.cn (Q.-Y. Liu).
Peer review under the responsibility of China University of Petroleum (Beijing).
[1] Fu-Li Wu and Qi-You Liu contributed equally to this manuscript.

https://doi.org/10.1016/j.petsci.2026.06.040
1995-8226/© 2026 The Authors. Publishing services by Elsevier B.V. on behalf of KeAi Communications Co. Ltd. This is an open access article under the CC BY-NC-ND license (http://creativecommons.org/licenses/by-nc-nd/4.0/).

biofilm erosion (Guo et al., 2024; Zhao et al., 2025). Nanomaterials have attracted increasing attention due to their high specific surface area and tunable antimicrobial properties. Zinc oxide nanoparticles (ZnO NPs) show potential in mitigating microbiologically influenced corrosion (MIC) through broad-spectrum antimicrobial activity (via Zn^{2+} release and reactive oxygen species) and chemical stability (Gudkov et al., 2021). However, conventional chemical synthesis of ZnO NPs relies on toxic reductants (e.g., hydrazine) and energy-intensive processes, conflicting with green chemistry principles (Ščajev and Gogova, 2024; Wang et al., 2023b).

Green synthesis, using bioactive molecules from plant extracts as reducing and stabilizing agents, offers a sustainable alternative (Barzinjy and Azeez, 2020; Li et al., 2021). This approach has been successfully applied to produce various nanomaterials for MIC mitigation, such as silver nanoparticles (Ag NPs) with potent anti-SRB activity and iron oxide nanoparticles (Fe_3O_4 NPs) that reduce corrosion rates (Hu et al., 2022; Su et al., 2025). ZnO NPs offer superior biocompatibility compared to these materials (Ramesh et al., 2021). Despite the broad potential of green nanomaterials (summarized in Table S1), the exploration of green-synthesized ZnO NPs remains limited. In particular, the roles of well-defined crystalline structures and organic–inorganic hybrid interfaces formed by surface-bound biomolecules in enhancing interfacial interaction and anti-biofilm capability are not fully understood. Moreover, the inhibition mechanism of plant-derived ZnO NPs against SRB in oilfield pipelines and their long-term efficacy in anaerobic corrosive environments remain unclear, limiting practical engineering application.

Therefore, this study aims to fill these knowledge gaps by elucidating how the bio-organic interfaces of green-synthesized ZnO NPs enhance anti-biofilm and anticorrosion functions. ZnO NPs were fabricated using tomato peel extract (GS-ZnO NPs). Tomato processing generates substantial waste annually, and tomato peels are rich in bioactive compounds such as lycopene, chlorogenic acid, and flavonoid glycosides (Fattore et al., 2016). This approach enables waste resource utilization while improving NP dispersion and targeted antimicrobial properties through biomolecular coating (Ibne Shoukani et al., 2024). The anticorrosion and antibacterial performance of GS-ZnO NPs were systematically compared with chemically synthesized ZnO NPs, evaluating their effectiveness in SRB biofilm inhibition, corrosion rate reduction, and galvanic coupling corrosion mitigation. The morphology, crystalline phase, and surface chemistry of GS-ZnO NPs were characterized, and electrochemical impedance spectroscopy (EIS) was used to elucidate their corrosion protection efficacy in simulated anaerobic oil pipeline environments. Mechanistic studies revealed that phytochemical-functionalized surfaces of GS-ZnO NPs disrupt SRB cell membranes and DNA integrity, thereby inhibiting biofilm formation and microbial activity. This study provides a novel approach for developing environmentally compatible MIC inhibitors, aligning with the energy industry's needs for decarbonization and circular economy.

2. Materials and methods

2.1. Materials

Tomato peel was purchased from a local market in Qingdao, China. Carbon steel sheets (10 × 10 × 2 mm and 40 × 10 × 2 mm) were supplied by Dongguan Yigang Metal Materials Co., Ltd. (Guangzhou, China). Zinc nitrate and chemically synthesized ZnO NPs were purchased from Sinopharm Chemical Reagent Co. Postgate medium and sodium D-lactate for SRB culture were obtained from Qingdao Hope Biotechnology Co. SRB strains were enriched from extracted water of the Tianjin offshore oil field. All reagents and culture media were prepared using ultrapure water (18.25 MΩ·cm).

2.2. Synthesis of zinc oxide nanoparticles

2.2.1. Preparation of pericarp extracts

Tomato peel was washed, cut, dried at 60 °C for 24 h, and ground into powder. For extraction, 10.0 g of dried powder was mixed with 500 mL distilled water (1:50 w/v), stirred at 300 rpm for 1 h at room temperature, then heated in a water bath at 60 ± 2 °C for 60 min. After cooling, the suspension was filtered through double-layer gauze. The extract (pH 4.3) was used directly without concentration. Its phytochemical composition was characterized in our prior work by liquid chromatography-mass spectrometry (LC–MS) (Wu et al., 2025), confirming the presence of key reducing and capping agents such as flavonoids and phenolic amides (e.g., feruloyltyramine).

2.2.2. Synthesis of ZnO NPs

ZnO nanoparticles were synthesized by dissolving 5 g of zinc nitrate in 200 mL of extract. The mixture was stirred well and then boiled on a heating plate to remove water to form a dark brown foam. The foam spontaneously combusted to produce an off-white powder, which was subsequently calcined at 400 °C for 1 h to obtain ZnO nanoparticles (Rashid et al., 2024). The pathway diagram illustrating the synthesis of ZnO nanoparticles stabilized by phytochemicals present in tomato peel extract is provided in Fig. S1.

2.3. Characterization of ZnO nanoparticles

The structural, morphological, and optical properties of the synthesized ZnO NPs were characterized by multiple techniques. UV–Vis spectroscopy (TU-1901, China) was performed in the wavelength range of 200–800 nm at a scan rate of 200 nm/min and a resolution of 1 nm using deionized water as reference. Fourier transform infrared spectroscopy (FTIR, Nicolet iS50, Thermo Scientific) was conducted via the KBr pellet method over 400–4000 cm^{-1} with a resolution of 0.5 cm^{-1} to identify functional compounds. X-ray diffraction (XRD, X'Pert PRO MPD, The Netherlands) was used to examine crystal structure and phase composition, with continuous scanning from 5° to 80° (2θ) at a rate of 7.5 °/min. Morphological features and particle size distribution were investigated by scanning electron microscopy (SEM, JSM-7800F, Japan) and transmission electron microscopy (TEM, JEM-2100F, Japan). Energy-dispersive X-ray spectroscopy (EDS) was performed to confirm elemental composition.

2.4. SRB culture

The sulfate-reducing bacteria (SRB) consortium used in this study was an oilfield-originated mixed culture, originally enriched from reinjection water of an oilfield operated by the Tianjin branch of CNOOC (China) Co. Enrichment was performed using a modified Postgate's C medium (detailed in the supplementary materials). The medium was adjusted to pH 7.5 with 1 N NaOH, purged with nitrogen for 20 min to establish anaerobic conditions, and autoclaved at 120 °C and 15 psi for 20 min. Enrichment was conducted in 250 mL anaerobic glass bottles at 35 °C with shaking at 110 rpm. Subculturing was performed weekly under strictly anaerobic conditions. After three months of successive enrichment, a highly active SRB mixed culture was obtained and used for corrosion inhibition experiments (Rasool et al., 2018). The community composition of SRB has been previously analyzed and reported (Su et al., 2024).

2.5. Bacteriostatic properties test

2.5.1. Quantitative PCR quantification and MIC determination

Sulfate-reducing bacteria (SRB) were inoculated into simulated reinjection water based on the water quality analysis of the Boxi operational area (China National Offshore Oil Corporation, Tianjin; Report No. GDGCBXW-2212-14). ZnO NPs synthesized from different precursors were added, and the systems were cultured anaerobically for 7, 14, 21, and 28 days. At each time point, samples were pretreated to exclude dead bacterial DNA: 5 μL of propidium monoazide (PMA) solution (1 mg/mL in dimethyl sulfoxide) was added to the sample, incubated in the dark for 5 min, and exposed to strong light for 20 min. A 5 mL aliquot was filtered through a 0.22 μm membrane to collect bacteria. The membrane was transferred to a 2 mL tube with 1 mL TE buffer, heated at 95 °C for 10 min to release DNA, and centrifuged to obtain the DNA template. Quantitative PCR (qPCR) targeting the dsrA gene was performed using SYBR Green master mix on a QuantStudio™ 3 system. Ct values were used to calculate absolute SRB quantities.

The antibacterial activity of ZnO NPs was evaluated by the minimum inhibitory concentration (MIC) method. ZnO NPs derived from tomato peel extract were added to Postgate's C medium via two-fold serial dilution to final concentrations of 500–1.95 μg/mL (Su et al., 2025; Wiegand et al., 2008). Enriched SRB cultures were inoculated and incubated anaerobically at 37 °C for 7 days, after which bacterial growth was assessed by optical density at 600 nm.

2.5.2. Staining of live and dead cells

Confocal laser scanning microscopy (CLSM, Zeiss LSM900) with dual-fluorescence staining was used for three-dimensional biofilm characterization. After 28 days of incubation in SRB-containing simulated reinjection water, carbon steel specimens were rinsed with phosphate-buffered saline (PBS) to remove planktonic cells and stained in the dark for 20 min using a SYTO-9/PI kit (SYTO-9 for live cells, green; propidium iodide for dead cells, red). After air-drying, samples were scanned at excitation wavelengths of 488 nm (SYTO-9) and 561 nm (PI) (Wang et al., 2023a). Acquired images were reconstructed to reveal the three-dimensional spatial distribution of live/dead bacteria and extracellular polymeric substances (EPS). The red-to-green fluorescence intensity ratio was used to quantitatively evaluate biofilm integrity and assess the antibacterial and corrosion-inhibition performance of the ZnO nanoparticles.

2.6. Weight loss

To evaluate the corrosion rate, specimens with dimensions of 40 mm × 10 mm × 2 mm were subjected to a weight loss test. Prior to exposure, the initial weights of three parallel samples (W_1) were recorded. After 28 days of incubation, corrosion products and biofilms were removed in accordance with ASTM G1–03, using a stannous chloride–hydrochloric acid solution. The final weight (W_2) was then measured using an electronic balance with a precision of 0.1 mg. The weight loss was calculated using Eq. (1) (Li et al., 2024):

$$W = \frac{W_1 - W_2}{S} \tag{1}$$

where S represents the exposed surface area. The corrosion inhibition efficiency (η) under biocide-treated conditions was determined using Eq. (2):

$$\eta = \frac{CR_{(untreated)} - CR_{(withtreated)}}{CR_{(untreated)}} \tag{2}$$

2.7. Electrochemical studies

Electrochemical measurements were performed using a Gamry Reference 600 P workstation (CHI660E, Shanghai) in a standard three-electrode configuration. Samples were immersed for 4, 7, 14, 21, and 28 days. Prior to electrochemical impedance spectroscopy (EIS), the system was maintained at open circuit potential (OCP) for 30 min to reach a steady state. EIS was conducted at OCP with a 5 mV sinusoidal perturbation over a frequency range of 100 kHz to 10 mHz. After 28 days of immersion, potentiodynamic polarization curves were recorded at a scan rate of 0.5 mV/s from −500 mV to +500 mV versus saturated calomel electrode (SCE) (Li et al., 2024; Rasheed et al., 2019; Yang et al., 2022). All measurements were performed in simulated oilfield refill water at 37 °C and repeated three times to ensure reproducibility.

2.8. Biofilm and corrosion morphology characterizations

To investigate the surface morphology and corrosion products of X65 carbon steel after 28 days of immersion in simulated oilfield reinjection water, specimens were characterized by scanning electron microscopy (SEM, XL80, FEG, Netherlands) at Ukeyan Laboratories (http://www.ukeyan.com). Samples were rinsed with phosphate-buffered saline (PBS, pH 7.4) to remove planktonic cells, then fixed with 4% (v/v) glutaraldehyde for 12 h and dehydrated through a graded ethanol series (50%, 60%, 70%, 90%, and 100%), each for 10 min. Energy-dispersive X-ray spectroscopy (EDS) was used to determine the elemental composition of corrosion products and biofilm-associated deposits. After corrosion tests, residual corrosion products were removed with a freshly prepared acid-cleaning solution. Cleaned steel surfaces were examined by SEM to assess corrosion features, and overall corrosion morphology was further analyzed using an ultra-depth-of-field optical microscope.

2.9. Testing of GS-ZnO NPs for damage to SRB bacteria

To investigate the cellular damage induced by green-synthesized ZnO nanoparticles on sulfate-reducing bacteria (SRB), ZnO NPs at 250 μg/mL were added to anaerobic medium and SRB were cultured at 37 °C for 7 days. The micro-morphology and structural integrity of SRB cells were examined by scanning electron microscopy (SEM) and transmission electron microscopy (TEM). DNA was extracted from untreated SRB cells and those treated with ZnO NPs synthesized via different methods after 7 days of culture using a DNA Extraction Kit. Extracted DNA was analyzed by gel electrophoresis at a constant voltage of 110 V. DNA damage was assessed by visualizing the gel under blue light and capturing images to observe band patterns.

2.10. Statistical analysis

All data are presented as mean ± standard deviation (SD) from at least three independent experiments ($n \geq 3$). Statistical significance was determined using GraphPad Prism 10.1.2. Comparisons among multiple groups were analyzed by one-way ANOVA followed by Tukey's post hoc test. A P-value <0.05 was considered statistically significant ($^*p < 0.05$, $^{**}p < 0.01$, $^{***}p < 0.001$, $^{****}p < 0.0001$).

3. Results and discussions

3.1. Characterization of ZnO NPs

The size, shape and morphology of ZnO nanoparticles biosynthesized using tomato peels were characterized using scanning electron microscopy and transmission electron microscopy. SEM and TEM analysis (Fig. 1(a) and (b)) revealed that the biosynthesized ZnO NPs are monodisperse quasi-spherical particles with well-defined hexagonal faceting, characteristic of wurtzite crystal formation. High-resolution statistical analysis of 200 particles demonstrated narrow size distribution (32.5 ± 1.59 nm), with 90% of particles falling within 25–45 nm range—an optimal size regime for biofilm penetration in pipeline systems (Fig. 1(d)) (Lahiri et al., 2021; Sachin et al., 2023).

EDS quantitative analysis (Fig. 1(c)) revealed a Zn:O atomic ratio of 41.7:58.3. This deviation from the ideal stoichiometric ratio may be attributed to the surface adsorption of oxygen-rich organic

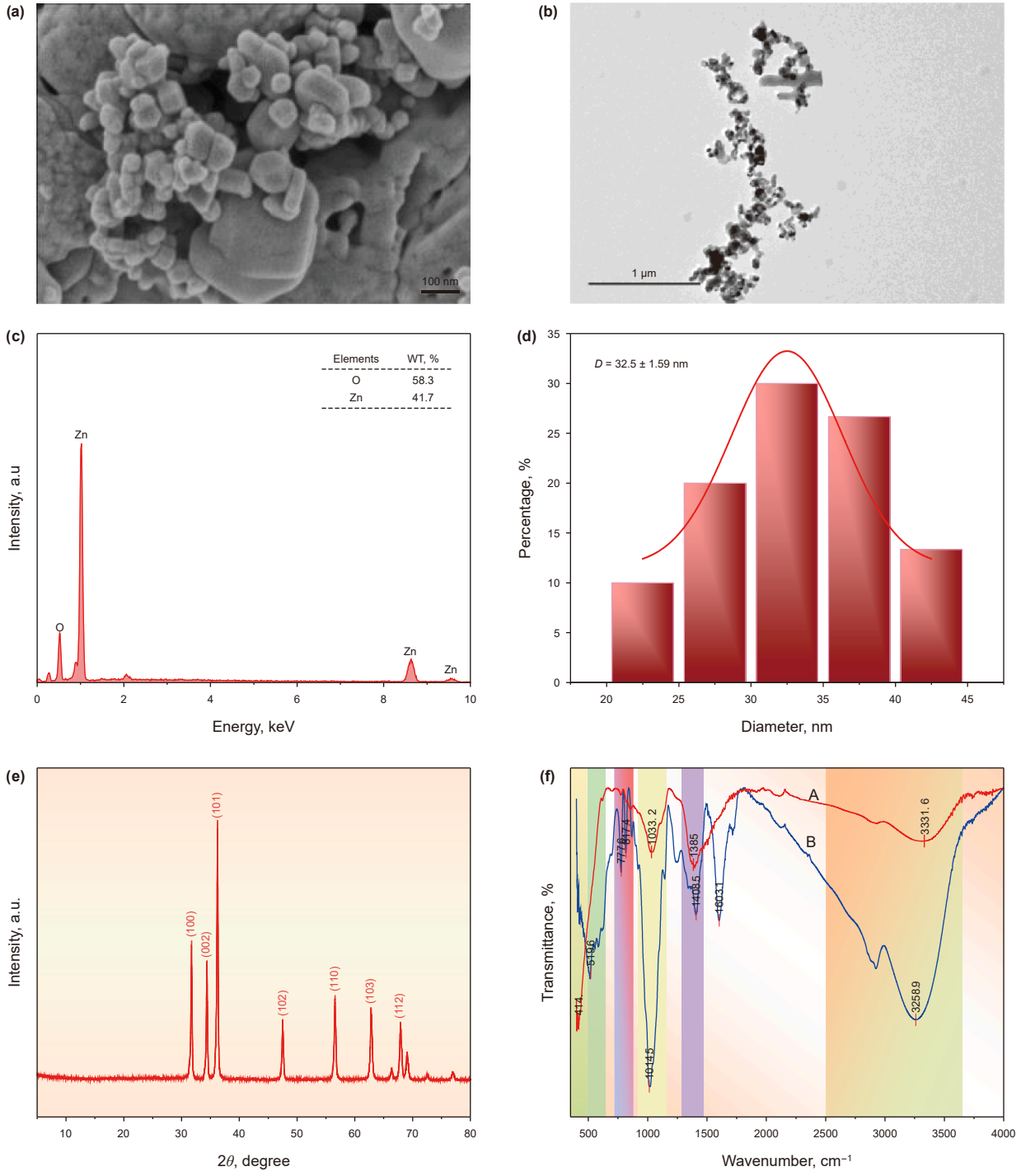


Fig. 1. Characterizations of ZnO NPs. (**a**) SEM image of ZnO nanoparticles at 100 nm scale. (**b**) TEM image of ZnO nanoparticles at 1 μm scale. (**c**) SEM-EDS elemental mapping of the synthesized ZnO nanoparticles. (**d**) Particle size distribution of ZnO nanoparticles at 50 nm scale. (**e**) XRD pattern of the synthesized ZnO nanoparticles. (**f**) FTIR spectra of ZnO nanoparticles synthesized from tomato peel extract (A) and pristine tomato peel extract (B).

ligands—such as citric acid and polyphenols—derived from the tomato peel extract used in the green synthesis. Functional groups like carbonyl (C=O) and hydroxyl (–OH) present in these organic compounds can contribute additional oxygen signals in the EDS measurement. This interpretation is further supported by the FTIR analysis, which confirmed the presence of these functional groups on the nanoparticle surface.

The crystalline structure of the synthesized ZnO nanoparticles was confirmed by XRD analysis. As illustrated in Fig. 1(e), the XRD pattern displayed prominent diffraction peaks at 2θ values of 31.7°, 34.4°, 36.2°, 47.5°, 56.6°, 62.8°, and 67.9°, corresponding to the (100), (002), (101), (102), (110), (103), (112), and (201) crystal planes, respectively. These diffraction peaks were characteristic of crystalline zinc oxide and closely matched the standard JCPDS card No. 36-1451, thereby confirming the formation of ZnO nanoparticles with a hexagonal wurtzite crystal structure (Zhu et al., 2021).

The FTIR spectrum of biosynthesized ZnO NPs (Fig. 1(f)) reveals both preservation of botanical components and evidence of phase transformation. Three principal modifications were observed: (1) The broad hydroxyl stretching band shifted from 3258 cm^{-1} to 3331 cm^{-1} with attenuated intensity, indicating Zn^{2+} chelation by catechol/phenolic groups of polyphenols (e.g., quercetin) and phenolic amides (e.g., feruloyltyramine) (Zhu et al., 2021). (2) Retained C–H vibrations at 2922/2918 cm^{-1} confirm adsorption of aliphatic compounds (e.g., palmitic acid, terpenoids) via hydrophobic interactions (Sachin et al., 2023), while the disappearance of the ester carbonyl peak near 1603 cm^{-1} suggests involvement of ester-containing compounds (e.g., feruloyltyramine) in reduction or surface binding (Sharma et al., 2020). (3) Emerging peaks at 1379 cm^{-1} and 414 cm^{-1} correspond to metal-coordinated phenolic C–O and Zn–O lattice vibrations, confirming successful biosynthesis (Arumugam et al., 2021). The persistent peak at 1034 cm^{-1}, assignable to glycosidic linkages, suggests carbohydrate-assisted stabilization. These signatures reveal a hierarchical coordination mechanism: polyphenols and phenolic amides initiate chelation; aliphatic compounds assist reduction and adsorption; saccharide derivatives and sphingolipids contribute to colloidal stability. The retention of these functional groups confirms a well-defined organic–inorganic hybrid interface that enhances dispersibility and biofilm penetration.

3.2. Weight loss and cells count

To evaluate the long-term corrosion inhibition performance of GS-ZnO NPs in comparison with CS-ZnO NPs, weight loss measurements and qPCR targeting SRB were conducted under simulated oilfield reinjection water conditions. As shown in Fig. 2(a), after 7 days of immersion in SRB-inoculated medium, unprotected carbon steel exhibited a weight loss of (3.74 ± 0.211) mg/cm^2. Upon addition of 250 ppm CS-ZnO NPs and GS-ZnO NPs, weight losses were reduced to (1.53 ± 0.174) mg/cm^2 and (0.82 ± 0.177) mg/cm^2, respectively, corresponding to corrosion inhibition efficiencies of approximately 59.1% and 78.1% (triplicate measurements provided in Table S3). Extended incubation to 28 days (Fig. 2(b)) revealed a more pronounced corrosion effect in the untreated group, with a weight loss of (9.58 ± 0.586) mg/cm^2. CS-ZnO NPs and GS-ZnO NPs reduced this loss to (4.71 ± 0.229) mg/cm^2 and (2.47 ± 0.171) mg/cm^2, respectively, indicating sustained and superior protection by GS-ZnO NPs over time. These results suggest that GS-ZnO NPs initiate rapid corrosion suppression and maintain long-term protection, likely due to better nanoparticle dispersion and biofilm resistance enhanced by bioactive compounds from the fruit extracts.

Quantification of SRB population dynamics was performed using fluorescence-based qPCR targeting SRB-specific genes. Fig. 2(c) and (d) present Ct values and calculated SRB cell counts after 7 and 28 days. At day 7, the SRB population in the untreated system peaked at approximately 4.9 × 10^5 cells/mL. With CS-ZnO NPs and GS-ZnO NPs, SRB counts dropped to 1.2 × 10^5 and 4.8 × 10^4 cells/mL, respectively. The SRB growth curves derived from Ct values (Fig. 2(e)) follow a classical bacterial growth profile (lag → log → stationary → death) (Rasheed et al., 2019), with corresponding data in Table S4. The presence of ZnO NPs significantly altered this trajectory by suppressing exponential growth and accelerating decline, with GS-ZnO NPs showing one-order-of-magnitude greater suppression than CS-ZnO NPs.

The minimum inhibitory concentration (MIC) against SRB was determined using a standard twofold dilution method (Hu et al., 2022; Su et al., 2025). As shown in Fig. 2(f), complete growth inhibition was achieved at 15.56 μg/mL, indicating high antimicrobial efficacy at low dosages. Collectively, both GS-ZnO NPs and CS-ZnO NPs exhibit significant antimicrobial and anticorrosion properties; however, GS-ZnO NPs consistently outperform CS-ZnO NPs across all tested metrics—corrosion mass loss, SRB inhibition, and MIC. The enhanced performance of GS-ZnO NPs is attributed to bio-organic molecules from tomato peel extracts, which act as capping agents to improve dispersion and synergistically enhance antimicrobial activity (Ahmed et al., 2017). These results highlight the dual functionality of GS-ZnO NPs as eco-friendly corrosion inhibitors and effective antimicrobial agents, offering a sustainable approach for microbial corrosion management in oilfield reinjection systems.

3.3. Live and dead cell staining

CLSM fluorescence imaging was used to evaluate the inhibitory effects of ZnO NPs on SRB biofilm formation on X65 carbon steel after 28 days of incubation in simulated oilfield reinjection water (Fig. 3). Red fluorescence indicates cell death, while green fluorescence represents live cells. In the blank control group (Fig. 3(a1)–(c1)), a dense and mature biofilm was observed, with a maximum thickness of approximately 66.48 μm. Treatment with CS-ZnO NPs (250 ppm) reduced biofilm thickness to 42.94 μm, a 35.4% reduction relative to the blank (Fig. 3(a2)–(c2)). Notably, GS-ZnO NPs (Fig. 3(a3)–(c3)) further reduced thickness to approximately 21.63 μm, a 67.5% reduction. This significant suppression is attributed to the synergistic antibacterial mechanisms of GS-ZnO NPs, including Zn^{2+} release, reactive oxygen species (ROS) generation, and enhanced bioactivity from plant-derived polyphenolic compounds (Król et al., 2017). The superior antimicrobial performance of GS-ZnO NPs is linked to surface modification by phenols and polysaccharides from plant extracts (Tao et al., 2025), which enhance interaction with SRB cell membranes, promote targeted ROS release, and maintain better dispersion stability for sustained Zn^{2+} release (Paul et al., 2023). This study confirms the potential of green-synthesized ZnO NPs as effective corrosion inhibitors in the oil and gas industry, highlighting the synergy between their environmentally friendly properties and long-lasting antimicrobial effects.

3.4. SEM examination of corrosion products

The surface morphology of X65 carbon steel after 28 days of immersion under three conditions was examined by SEM, with elemental composition analyzed by EDS (Fig. 4). In the SRB control group (Fig. 4(a1)), extensive biofilm formation and dense corrosion products were observed, with spherical and rod-shaped bacterial colonies embedded in EPS—typical indicators of severe MIC (Chen

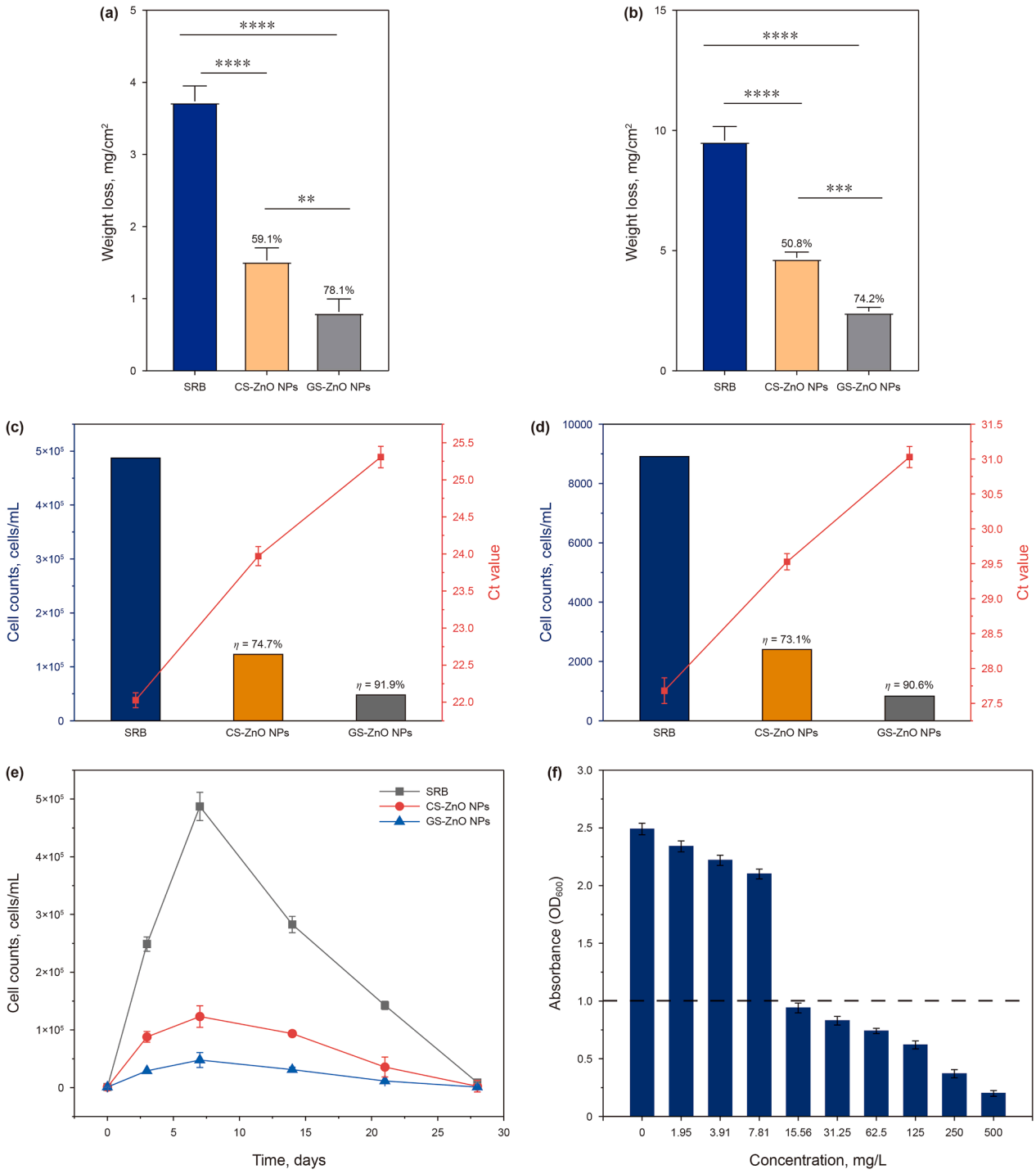


Fig. 2. (a–b) Weight loss of X65 carbon steel specimens after 7 and 28 days of immersion in simulated oilfield reinjection water. (**c–d**) Ct values and corresponding sulfate-reducing bacteria (SRB) counts determined by qPCR at 7 and 28 days, respectively. (**e**) Growth curve of planktonic SRBs under anaerobic conditions. (**f**) Minimum inhibitory concentration of ZnO nanoparticles synthesized from tomato peel extract against SRB.

and Zhang, 2018; Davidova and Lenhart, 2021; Jin et al., 2014). Upon treatment with CS-ZnO NPs (Fig. 4(b1)), biofilm coverage and corrosion product deposition were markedly reduced, although residual SRB structures and minor pitting remained. Notably, the GS-ZnO NPs group (Fig. 4(c1)) presented a mostly smooth, intact surface with minimal biofilm or corrosion product adherence, demonstrating superior antimicrobial and corrosion protection. EDS analysis revealed significant differences in zinc deposition. The control group contained only trace Zn (0.89 wt%). The CS-ZnO NPs group showed a Zn content of 9.66 wt%, while the GS-ZnO NPs group exhibited substantially higher Zn content of 30.75 wt% (Fig. 4(a2)–(c3)), indicating dense and stable surface coverage. The enhanced Zn loading on GS-ZnO NP-treated surfaces suggests that fruit peel extracts promote nanoparticle dispersion and stronger interactions with the steel substrate. Surface-bound ZnO NPs continuously release Zn^{2+} ions, disrupting bacterial

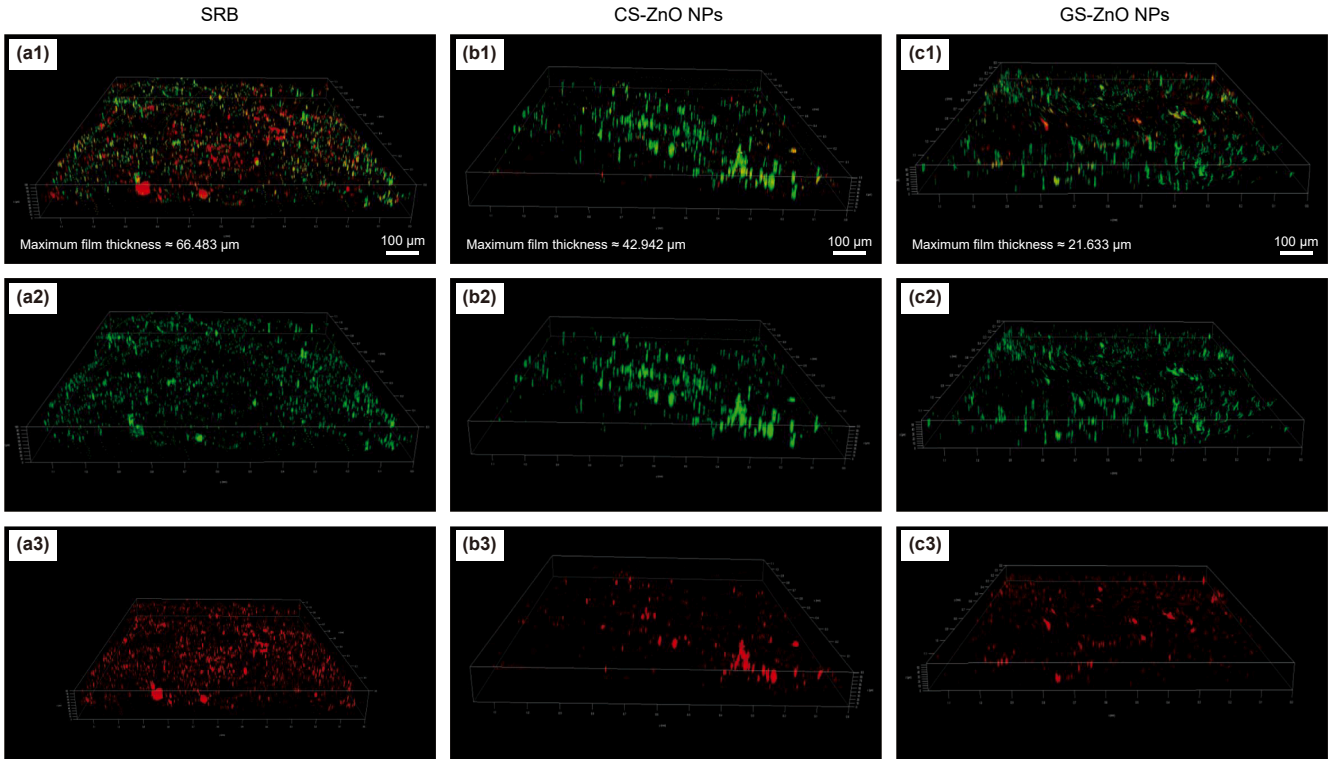


Fig. 3. 3D-CLSM images of live/dead cells in biofilms on X65 steel after 28 days of immersion under (**a1–a3**) SRB, (**b1–b3**) SRB + CS-ZnO NPs, (**c1–c3**) SRB + GS-ZnO NPs. The stained green and red colors in the images represent live and dead cells, respectively.

metabolism and membrane integrity, while also acting as a physical barrier that inhibits electron transfer essential for SRB-induced corrosion (Choi et al., 2010; Vielkind et al., 2013). Overall, these findings confirm the dual functionality of GS-ZnO NPs as effective antimicrobial agents and corrosion inhibitors, offering a promising and environmentally sustainable strategy for managing MIC in oilfield reinjection systems.

3.5. Electrochemical tests

Electrochemical impedance spectroscopy (EIS) is a key technique for investigating interfacial reactions and corrosion mechanisms at the metal/biofilm interface (Moradi et al., 2022). EIS spectra of carbon steel immersed in SRB-containing media for 4–28 days were compared among the blank, CS-ZnO NPs, and GS-ZnO NPs groups (Fig. 5). In the blank group (Fig. 5(a1)), the Nyquist plots exhibited the largest semicircle diameter at day 7, reflecting a temporary increase in charge transfer resistance (R_{ct}) due to the initial protective effect of the maturing SRB biofilm (Liu et al., 2015). The subsequent decrease in semicircle diameter indicated reduced R_{ct}, suggesting that biofilm degradation accelerated corrosion (Chongdar et al., 2005). In contrast, the addition of 250 μg/mL ZnO nanoparticles markedly increased the Nyquist semicircle diameter, with GS-ZnO NPs exhibiting superior performance (Fig. 5(a3)). After 7 and 28 days of immersion, GS-ZnO NPs increased R_{ct} by approximately 13-fold and 11-fold (Table S5), respectively, outperforming chemically synthesized ZnO NPs (Fig. 5(a2)) by approximately 7.8-fold, highlighting their enhanced corrosion inhibition capability.

The corresponding Bode phase diagrams are shown in Fig. 5(b1)–(b3) and (c1)–(c3). In Bode plots, the frequency and amplitude of the maximum phase angle (θ_{max}) reflect the dynamic evolution of the electrode/electrolyte interface (Lazanas and Prodromidis, 2023). The blank group (Fig. 5(c1)) exhibited typical Warburg impedance behavior in the low-frequency region, with a phase angle of approximately 45°, indicating a diffusion-controlled process. In contrast, the GS-ZnO NPs group (Fig. 5(c3)) showed a markedly different response (Yu et al., 2013), with a dense protective film forming on the metal surface that inhibited contact between SRB metabolites (e.g., H_2S, organic acids) and the substrate, thereby suppressing corrosion reactions and impeding charge transfer. This was reflected by a significant increase in R_{ct}, a phase angle approaching −90°, and a rightward shift of the characteristic frequency (Castaneda and Benetton, 2008), indicating a shift from diffusion-controlled to capacitance-dominated interfacial behavior. Fig. 6(a) and (b) present the equivalent circuit model used to interpret the EIS data, where R_s is solution resistance, Q_f and R_f are constant phase element and resistance of the surface film, Q_{dl} is the double-layer CPE, R_{ct} is charge transfer resistance, and W represents Warburg impedance. Corresponding fitting parameters are summarized in Table S5.

Fig. 6(c) presents the polarization curves of carbon steel samples subjected to different treatments after 28 days of immersion in simulated oilfield reinjection water. Table 1 summarizes the electrochemical parameters obtained from polarization curve fitting, including the corrosion potential (E_{corr}), corrosion current density (i_{corr}), and the anodic and cathodic Tafel slopes (β_a and β_c). As shown in Fig. 6(e), the blank group exhibited a high corrosion current density of 21.3 μA, indicating a rapid corrosion process. Upon the addition of ZnO nanoparticles, significant electrochemical changes were observed: Ecorr shifted positively, and the cathodic Tafel slope (β_c) increased notably, suggesting an effective suppression of the cathodic oxygen reduction reaction. Notably, the icorr decreased substantially to 9.9 μA with chemically synthesized ZnO nanoparticles and further to 8.6 μA with green-synthesized ZnO nanoparticles derived from tomato peel extract,

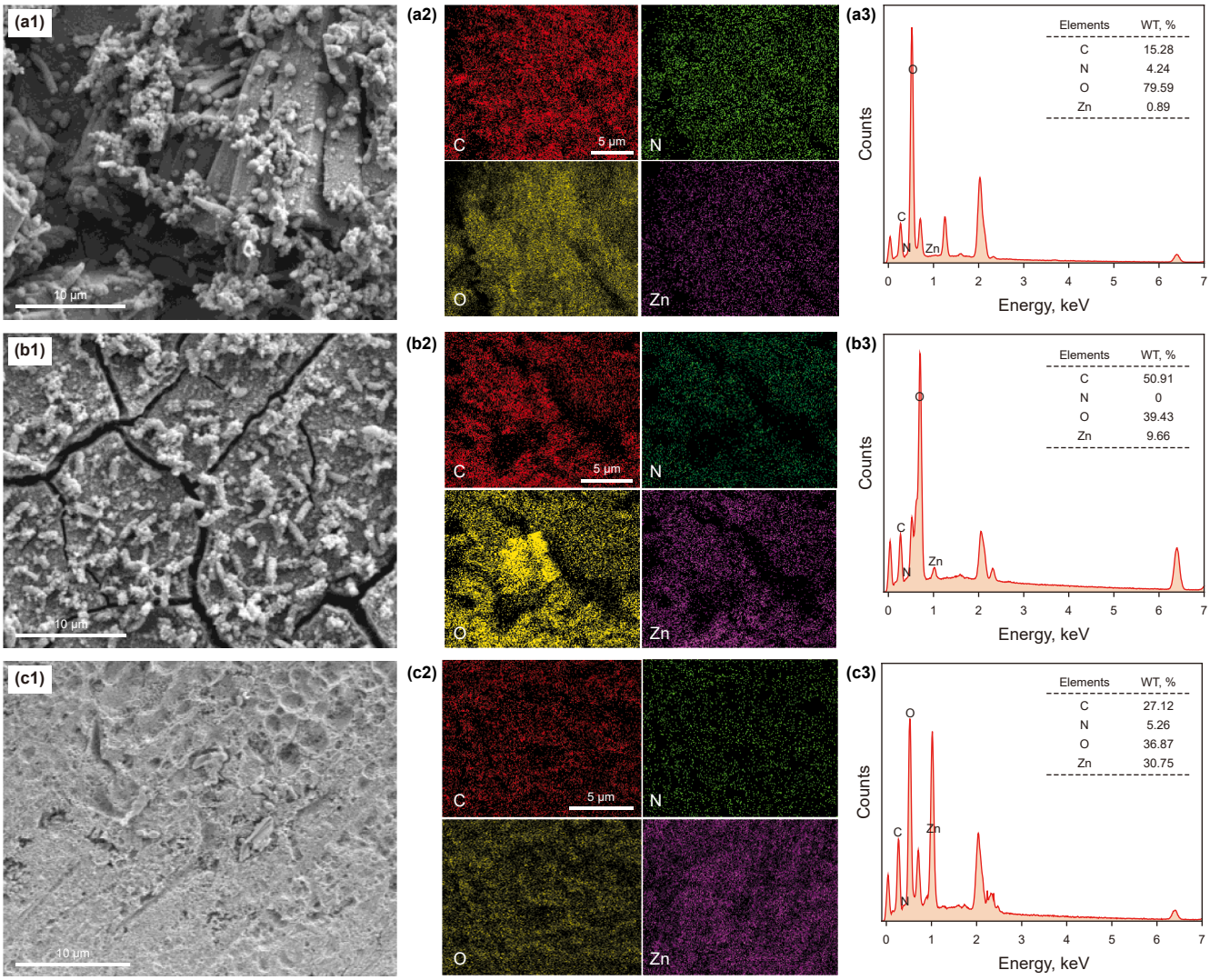


Fig. 4. SEM images, elemental distribution maps, and EDS analysis of biofilms formed on the steel surface after 28 days of SRB-induced corrosion. (**a1–c1**) Pure SRB group; (**a2–c2**) SRB + CS-ZnO NPs group; (**a3–c3**) SRB + GS-ZnO NPs group.

corresponding to corrosion inhibition efficiencies of approximately 53.5% and 59.6%, respectively. The formula for calculating the inhibitory effect of ZnO NPs on corrosion (Li et al., 2024):

$$\eta = \frac{(i_{corr})_{untreated} - (i_{corr})_{ZnO\ NPs}}{(i_{corr})_{untreated}} \times 100\% \quad (3)$$

These results underscore the enhanced inhibitory effect of green-synthesized ZnO NPs, which, through their interaction with biomolecules on the surface, promote rapid adsorption and the formation of a compact, protective passivation layer. Overall, the ZnO NPs, particularly those synthesized via green methods, exhibited superior corrosion resistance by effectively modulating the electrochemical behavior at the metal/biofilm interface.

As shown in Fig. 6(d), the initial open circuit potential (OCP) of GS-ZnO NPs was significantly higher than that of CS-ZnO NPs, attributed to rapid adsorption of surface-bound biomolecules (e.g., polyphenols, flavonoids) forming a transient passivation layer that suppresses initial corrosion (Oguzie, 2008). Over time, exposure to corrosive agents (e.g., Cl^-, H_2S) may cause partial dissolution or rearrangement of these biomolecules, leading to a temporary OCP decline (Lazrak et al., 2025). With continued immersion, ZnO NPs deposit and interact with corrosion products (e.g., FeS, Fe_2O_3) to form a stable protective film (Yang et al., 2022), while Zn^{2+} release inhibits SRB proliferation, contributing to a subsequent OCP rise. In contrast, CS-ZnO NPs exhibited a lower initial OCP that increased slowly, followed by gradual decline and stabilization, reflecting the absence of biomolecular components and a less synergistic protective effect.

Fig. 6(f) illustrates the time-dependent variation of R_{ct} on the iron surface, reflecting electron loss during corrosion. In all groups, R_{ct} increased during the first 7 days, reaching a maximum, and subsequently declined, attributed to the initial formation and later degradation of protective biofilms. Notably, the R_{ct} values in the GS-ZnO NPs group remained consistently higher than those of the CS-ZnO NPs and blank groups throughout immersion, indicating that green-synthesized ZnO NPs form a more stable and effective interfacial film, contributing to sustained corrosion inhibition.

3.6. Analysis of corrosion product removal

The corrosion inhibition mechanism of biosynthesized ZnO nanoparticles on X65 carbon steel in simulated oilfield reinjection water over 28 days is illustrated in Fig. 7. In the blank group (pure SRB system), the steel surface exhibited typical SRB corrosion

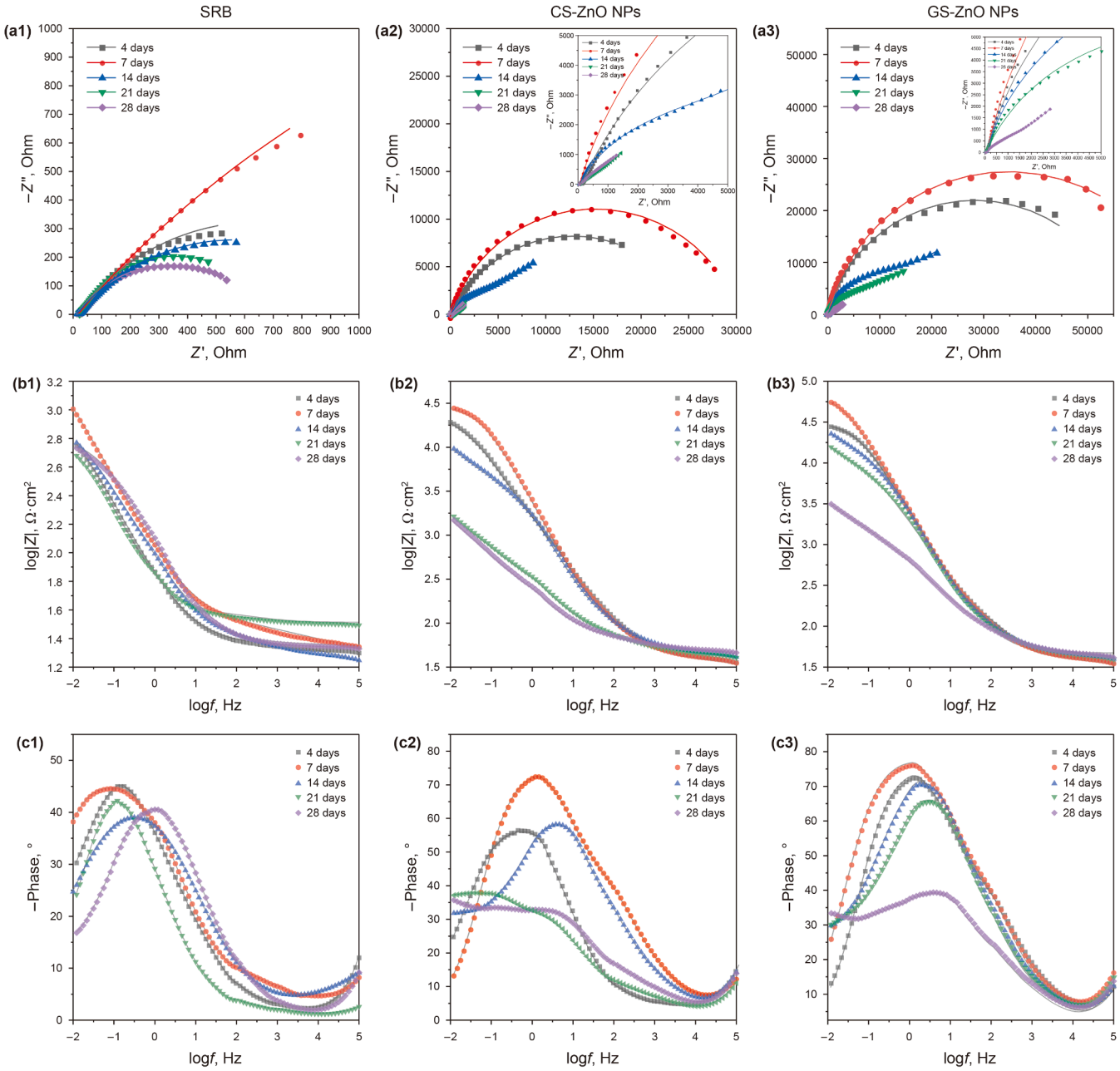


Fig. 5. Nyquist (**a1–a3**) and Bode (**b1–c3**) plots of X65 carbon steel after 28-day incubation in simulated oilfield reinjection water. The conditions are: (**a1**, **b1**) SRB only, (**a2**, **b2**) SRB with CS-ZnO NPs, and (**a3**, **c3**) SRB with GS-ZnO NPs.

patterns, including densely distributed mushroom-shaped pits (Fig. 7(a)), indicating that SRB metabolic activity induced local acidification and severe pitting corrosion (Mahanipour and Ghaedi, 2022). In the CS-ZnO NPs group (250 μg/mL), corrosion was significantly reduced although pits remained, suggesting that chemically synthesized ZnO nanoparticles partially inhibited SRB adhesion and proliferation through a physical barrier effect (Fig. 7(b)). In contrast, the GS-ZnO NPs group (250 μg/mL) displayed a uniformly passivated surface with no visible pits (Fig. 7(c)), demonstrating that biosynthesized ZnO nanoparticles effectively prevented SRB colonization and corrosion without relying solely on a physical barrier. These findings highlight the superior and more eco-friendly corrosion inhibition performance of GS-ZnO NPs compared to chemically synthesized alternatives.

Three-dimensional ultra-depth microscopy analysis (Fig. 8) revealed distinct localized corrosion features across treatment groups in the SRB-inoculated system (Li et al., 2020; Yang et al., 2022). The blank control group (Fig. 8(a)) exhibited severe microbial-induced pitting with a maximum pit depth of 25.77 μm and width of 123.28 μm (depth-to-width ratio ≈ 0.21), consistent with SRB-mediated local acidification. In contrast, GS-ZnO NPs (250 ppm) (Fig. 8(c)) demonstrated exceptional corrosion suppression, reducing the maximum pit depth to 4.14 μm (83.9% inhibition efficiency) with shallow dish-shaped pits (depth-to-width ratio ≈ 0.14), indicating marked suppression of corrosion propagation. CS-ZnO NPs (250 ppm) (Fig. 8(b)) achieved a maximum pit depth of 6.86 μm (73.3% inhibition efficiency, depth-to-width ratio ≈ 0.16), underperforming compared

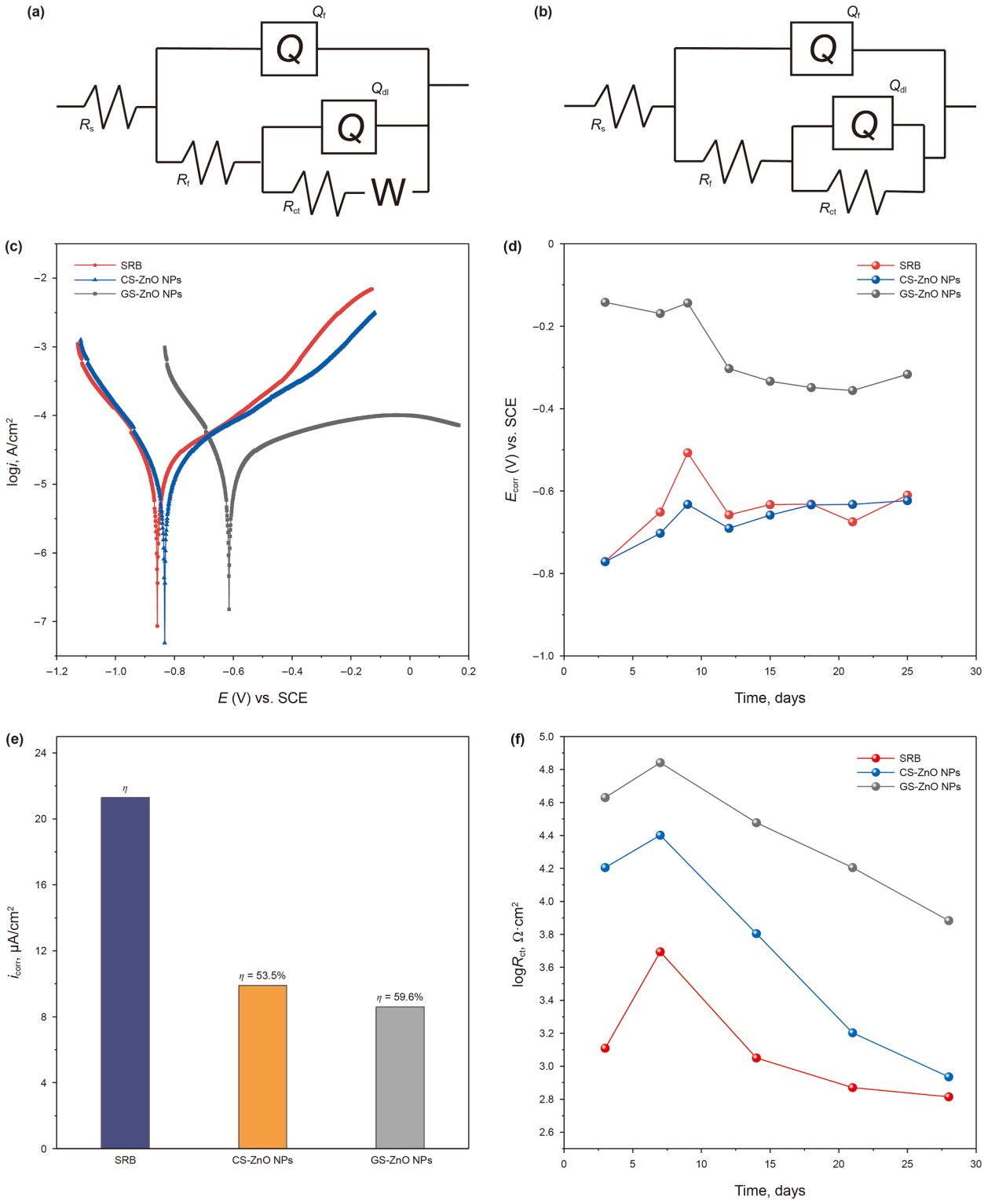


Fig. 6. (**a**) Equivalent circuit model used to fit EIS data for 14, 21, and 28 days of incubation. (**b**) Equivalent circuit model used for 4 and 7 days of incubation. (**c**) Potentiodynamic polarization curves of X65 carbon steel after 28 days of incubation with SRB under different conditions. (**d**) Evolution of open-circuit potential over time. (**e**) Corrosion current densities derived from polarization curves. (**f**) Temporal variation of R_{ct} calculated from EIS parameters.

to biosynthesized NPs by a 10.6% efficiency gap. These results quantitatively validate the superior interfacial activity and SRB-suppressing capability of phytochemical-functionalized ZnO NPs in mitigating localized MIC.

3.7. Mechanism of destruction of SRB by GS-ZnO NPs

To further investigate the inhibitory mechanisms of ZnO NPs, DNA gel electrophoresis was used to evaluate DNA damage in SRB,

Table 1
Tafel parameters fitted from potentiodynamic polarization curves.

Group	β_a, mV/dec	β_c, mV/dec	E_{corr} (mV) vs. SCE	i_{corr}, μA/cm^2	η
SRB	397	−179	−840	21.3	-
CS	211	−122	−838	9.9	53.5%
GS	164	−70.6	−623	8.6	59.6%

while SEM and TEM were employed to examine morphological and ultrastructural changes in treated cells (Fig. 9). SEM images (Fig. 9(a1)–(a3)) showed that untreated SRB cells appeared slightly curved, with intact surfaces and surrounding metabolites. In contrast, SRB cells treated with ZnO NPs (Fig. 9(b1)–(b3)) exhibited rough surfaces, pits, and cell breakage (red circles), with numerous ZnO NPs adsorbed onto cell surfaces (green circles). TEM images

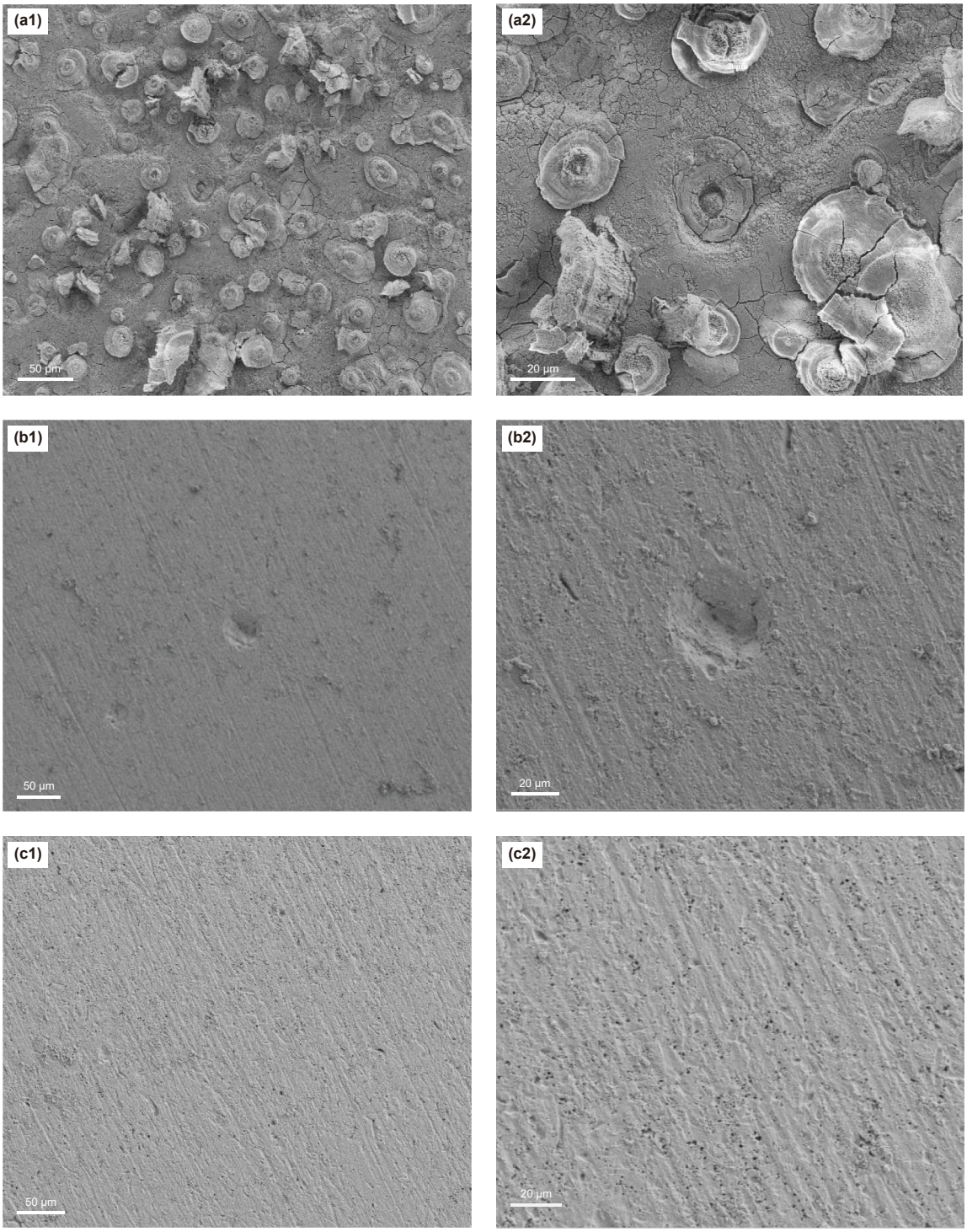


Fig. 7. SEM images of steel surfaces after removal of biofilms following 28 days of SRB-induced corrosion. (**a1–a2**) Pure SRB group; (**b1–b2**) SRB + CS-ZnO NPs group; (**c1–c2**) SRB + GS-ZnO NPs group.

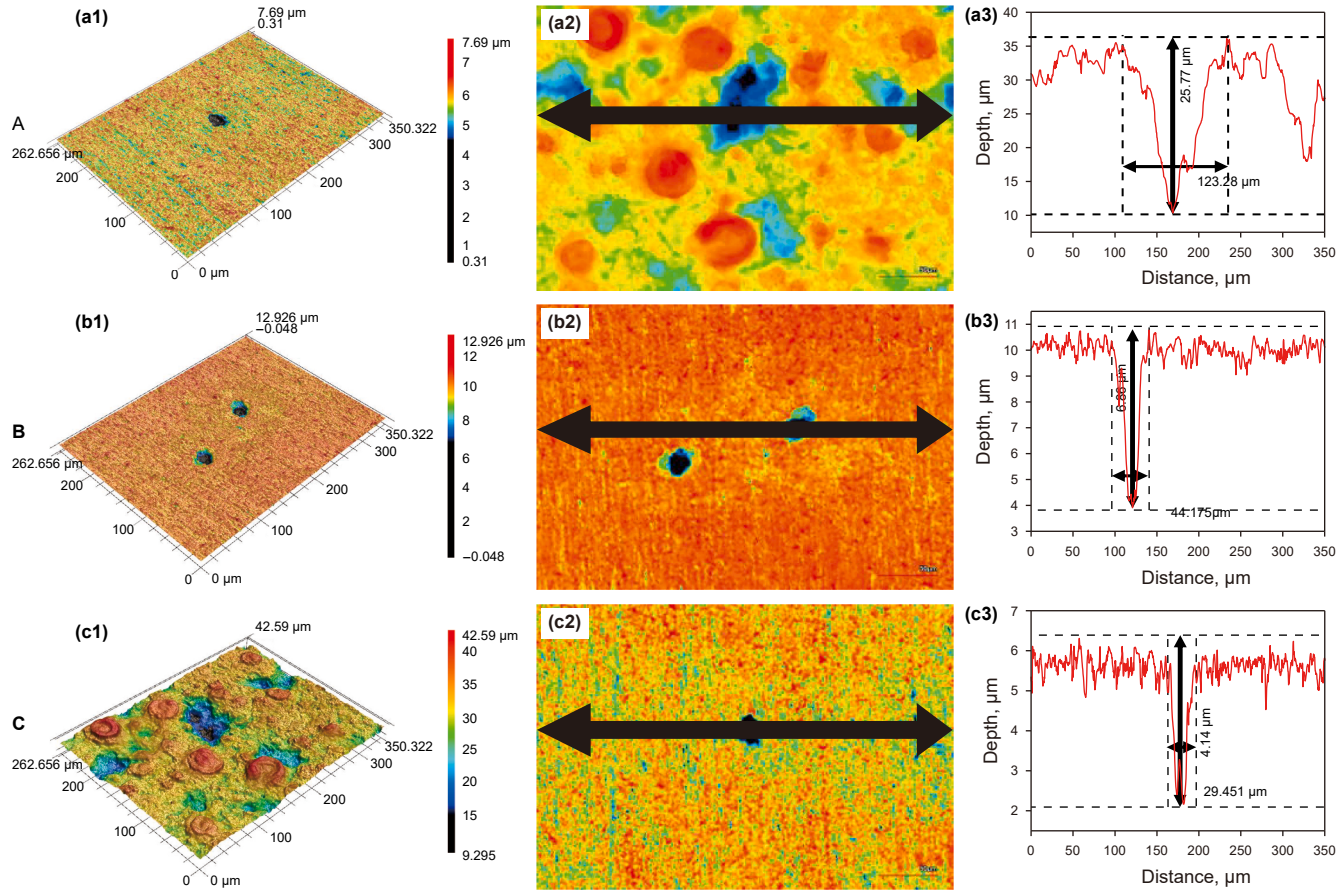


Fig. 8. 3D-VH and 2D-VH images of the deepest corrosion pits after removing the biofilms/corrosion products on X65 steel after 28 d immersion under (**a1–a3**) SRB, (**b1–b3**) SRB + CS-ZnO NPs, (**c1–c3**) SRB + GS-ZnO NPs. (**a3–c3**) show the 2D profile images of the black arrow in (**a2–c2**).

revealed that untreated SRB cells (Fig. 9(c1)–(c2)) had high density, intact membranes, and exocytosis of corrosion products (red arrow). After treatment (Fig. 9(c3)–(c4)), significant membrane rupture (blue circle) and cytoplasmic leakage (blue arrow) were observed. EDS analysis of TEM regions showed Zn and O absorption peaks (yellow dotted line), with weight percentages of 11.64% and 88.36%, respectively (Fig. 9(d2)). Elemental mapping (Fig. 9(d3)–(d4)) indicated Zn and O were evenly distributed inside and outside SRB cells, confirming nanoparticle adsorption and internalization. DNA gel electrophoresis (Fig. 9(d1)) showed that, unlike the clear genomic DNA bands of untreated SRB, ZnO NP-treated samples exhibited fainter and more diffuse bands. Collectively, these results demonstrate that ZnO NP internalization causes severe physical damage to SRB cells, compromising their viability.

3.8. Possible corrosion inhibition mechanism

Compared to other green nanomaterials for MIC mitigation—such as Ag NPs with high cost and potential ecotoxicity, or Fe_3O_4 NPs offering primarily barrier protection—the tomato peel-derived ZnO NPs in this work provide a superior combination of multi-mechanistic efficacy and environmental sustainability. A schematic overview of the proposed dual inhibition pathways is provided in Fig. 10. The superior corrosion mitigation performance of GS-ZnO NPs arises from the synergistic effects of electrochemical suppression and antibacterial activity. On the electrochemical level, phytochemical-derived surface functionalities (e.g., polyphenols, flavonoids) facilitate rapid adsorption onto the steel surface, forming a transient passivation layer that retards initial anodic dissolution. Over time, ZnO NPs interact with corrosion products (e.g., FeS, Fe_2O_3), contributing to a more adherent and stable protective film, as evidenced by significantly elevated R_{ct} and the transformation of pit morphology from deep localized attack to shallow, uniform depressions. The organic–inorganic hybrid interface enhances nanoparticle dispersion and interfacial adhesion, reducing localized electrochemical heterogeneity and suppressing pitting corrosion. From the antibacterial perspective, GS-ZnO NPs exhibit enhanced inhibition of SRB compared to chemically synthesized counterparts. Bioactive phytochemicals on the nanoparticle surfaces disrupt SRB cell membrane integrity, leading to cell deformation and metabolic inactivation, as confirmed by SEM analysis. Additionally, GS-ZnO NPs hinder SRB attachment and biofilm formation, reducing biofilm thickness by over 67.5%. This suppression of SRB colonization minimizes the production of corrosive metabolites (e.g., FeS), thereby mitigating microbial-induced acidification and localized corrosion. Collectively, the green-synthesized ZnO NPs provide dual-function protection by passivating the metal surface while disrupting microbial activity, underpinning their remarkable and long-lasting corrosion inhibition performance in anaerobic oilfield environments.

3.9. Scalability and cost considerations

The green synthesis route uses tomato peel—an abundant agricultural by-product—as a low-cost renewable feedstock,

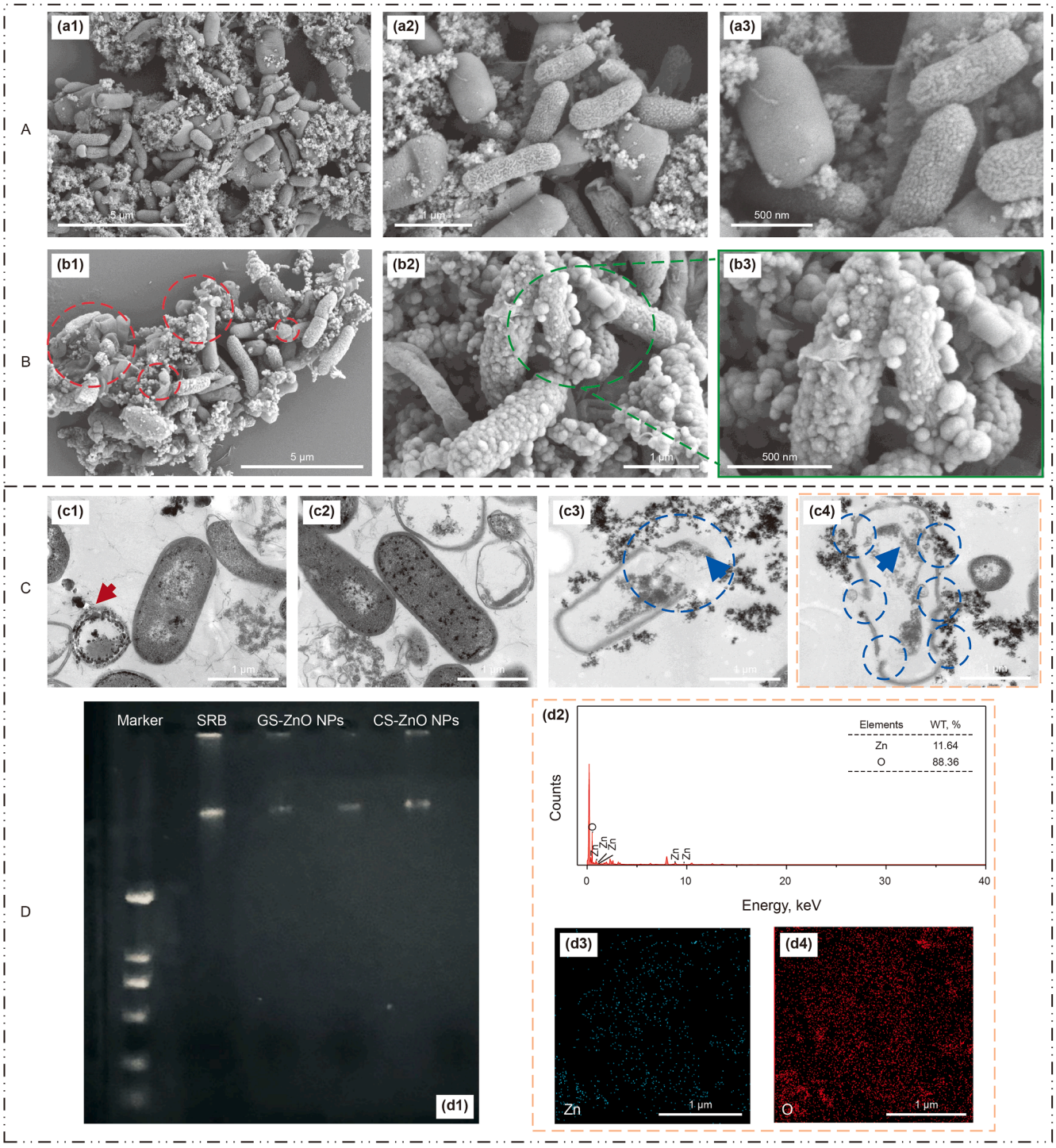


Fig. 9. SEM and TEM images of SRB cells untreated with GS-ZnO NPs (**a1–a3**) and (**c1–c2**) and SRB cells treated with GS-ZnO NPs (**b1–b3, c3–c4**). DNA electrophoresis results (**d1**). EDS images of SRB cells treated with GS-ZnO NPs (**d2–d4**).

offering a clear advantage over conventional precursors. The aqueous extraction and precursor formation steps are simple and conducted under mild conditions. Although subsequent calcination at 400 °C requires energy input, the overall process avoids expensive or highly toxic reagents, thereby reducing both chemical costs and environmental remediation concerns. This streamlined approach, which integrates biomass valorization with nanoparticle synthesis, provides a cost-effective and sustainable alternative to traditional inhibitors. However, the long-term environmental implications—particularly Zn^{2+} leaching and ecotoxicity—require thorough evaluation. As shown by the reduced acute aquatic toxicity of chitosan-capped ZnO nanoparticles, surface functionalization with biocompatible molecules underscores the critical role of a biomolecular corona (Rasool et al., 2021). Therefore, while the phytochemical capping used in this study suggests a favorable environmental profile, a dedicated assessment of long-term stability, ion release kinetics, and chronic environmental impact remains essential for future field application and scale-up.

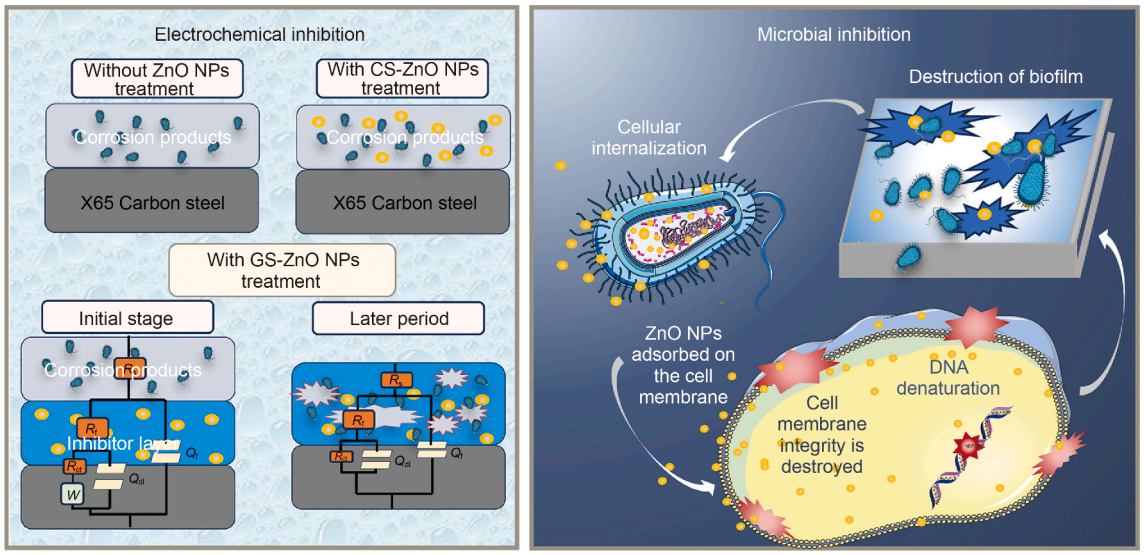


Fig. 10. Schematic illustration of the dual inhibition mechanisms of ZnO NPs.

4. Conclusions and recommendations

This study demonstrates the effectiveness of ZnO NPs green-synthesized from tomato peel extract as a sustainable solution to mitigate MIC in petroleum pipeline reinjection systems. Phytochemical-assisted synthesis produced well-dispersed, wurtzite-structured ZnO NPs with enhanced interfacial activity and strong biofilm penetration. The green-synthesized ZnO NPs achieved a 90.6% reduction in viable SRB cells, a 74.2% reduction in corrosion rate based on weight loss, and an 83.9% decrease in maximum pit depth. Biofilm formation was inhibited by 67.5% based on CLSM quantification. Electrochemical impedance spectroscopy revealed that green ZnO NPs increased R_{ct} by approximately 13-fold and 11-fold after 7 and 28 days, respectively—outperforming chemically synthesized counterparts by approximately 7.8 times. Future studies should focus on systematic dose-response investigations to determine the optimal concentration of GS-ZnO NPs, as well as validation in dynamic flow-loop systems with authentic field-produced water. A limitation of this study is that experiments were conducted under controlled, static anaerobic conditions, which may not fully capture the dynamic flow and complex chemistry of real pipeline environments. Additionally, potential variability in the phytochemical composition of tomato peel extract due to seasonal or sourcing factors was not investigated.

CRediT authorship contribution statement

Fu-Li Wu: Writing – original draft, Methodology, Data curation. **Qi-You Liu:** Supervision, Resources, Funding acquisition. **Yu-Hua Su:** Methodology. **Guang-Lei Lv:** Resources. **Peng Xiao:** Data curation. **Lei Lu:** Methodology. **Yong-Qiang Wang:** Data curation. **Gang Wang:** Methodology.

Declaration of competing interest

The authors declare that they have no known competing financial interests or personal relationships that could have appeared to influence the work reported in this paper.

Acknowledgements

This work was financially supported by State Key Laboratory of Heavy Oil Processing and Fundamental Research Funds for the Central University (Grant No. 24CX02020A).

Supplementary data

Supplementary data to this article can be found online at https://doi.org/10.1016/j.petsci.2026.06.040.

References

Ahmed, S., Annu, Ali, Chaudhry, S., et al., 2017. A review on biogenic synthesis of ZnO nanoparticles using plant extracts and microbes: a prospect towards green chemistry. J. Photochem. Photobiol. B Biol. 166, 272–284. https://doi.org/10.1016/j.jphotobiol.2016.12.011.

Arumugam, M., Manikandan, D.B., Dhandapani, E., et al., 2021. Green synthesis of zinc oxide nanoparticles (ZnO NPs) using Syzygium cumini: potential multi-faceted applications on antioxidants, cytotoxic and as nanonutrient for the growth of Sesamum indicum. Environ. Technol. Innov. 23, 101653. https://doi.org/10.1016/j.eti.2021.101653.

Barzinjy, A.A., Azeez, H.H., 2020. Green synthesis and characterization of zinc oxide nanoparticles using Eucalyptus globulus Labill. Leaf extract and zinc nitrate hexahydrate salt. SN Appl. Sci. 2 (5), 991. https://doi.org/10.1007/s42452-020-2813-1.

Castaneda, H., Benetton, X.D., 2008. SRB-biofilm influence in active corrosion sites formed at the steel-electrolyte interface when exposed to artificial seawater conditions. Corros. Sci. 50 (4), 1169–1183. https://doi.org/10.1016/j.corsci.2007.11.032.

Chen, S., Zhang, D., 2018. Study of corrosion behavior of copper in 3.5 wt.% NaCl solution containing extracellular polymeric substances of an aerotolerant sulphate-reducing bacteria. Corros. Sci. 136, 275–284. https://doi.org/10.1016/j.corsci.2018.03.017.

Choi, E.K., Lee, H.H., Kang, M.S., et al., 2010. Potentiation of bacterial killing activity of zinc chloride by pyrrolidine dithiocarbamate. J. Microbiol. 48 (1), 40–43. https://doi.org/10.1007/s12275-009-0049-2.

Chongdar, S., Gunasekaran, G., Kumar, P., 2005. Corrosion inhibition of mild steel by aerobic biofilm. Electrochim. Acta 50 (24), 4655–4665. https://doi.org/10.1016/j.electacta.2005.02.017.

Davidova, I.A., Lenhart, T.R., et al., 2021. Composition and corrosivity of extracellular polymeric substances from the hydrocarbon-degrading sulfate-reducing bacterium desulfoglaeba alkanexedens ALDC. Microorganisms 9 (9), 1994. https://doi.org/10.3390/microorganisms9091994.

Fattore, M., Montesano, D., Pagano, E., et al., 2016. Carotenoid and flavonoid profile and antioxidant activity in "Pomodorino Vesuviano" tomatoes. J. Food Compos. Anal. 53, 61–68. https://doi.org/10.1016/j.jfca.2016.08.008.

Gudkov, S.V., Burmistrov, D.E., Serov, D.A., et al., 2021. A mini review of antibacterial properties of ZnO nanoparticles. Front. Phys. 9, 641481. https://doi.org/10.3389/fphy.2021.641481.

Guo, Z., Xiao, Z., Chen, H., et al., 2024. Review of cathodic protection technology for steel rebars in concrete structures in marine environments. Appl. Sci. 14 (19), 9062. https://doi.org/10.3390/app14199062.

Hu, Y., Feng, Q., Zeng, H., et al., 2022. Corrosion inhibition of sulphate-reducing bacterial by Ag/Cu bimetallic nanoparticles synthesised from ginger extract. J. Clean. Prod. 377, 134204. https://doi.org/10.1016/j.jclepro.2022.134204.

Ibne Shoukani, H., Nisa, S., Bibi, Y., et al., 2024. Ciprofloxacin loaded PEG coated ZnO nanoparticles with enhanced antibacterial and wound healing effects. Sci. Rep. 14, 4689. https://doi.org/10.1038/s41598-024-55306-z.

Jia, R., Unsal, T., Xu, D., et al., 2019. Microbiologically influenced corrosion and current mitigation strategies: a state of the art review. Int. Biodeterior. Biodegrad. 137, 42–58. https://doi.org/10.1016/j.ibiod.2018.11.007.

Jin, J., Wu, G., Zhang, Z., et al., 2014. Effect of extracellular polymeric substances on corrosion of cast iron in the reclaimed wastewater. Bioresour. Technol. 165, 162–165. https://doi.org/10.1016/j.biortech.2014.01.117.

Król, A., Pomastowski, P., Rafińska, K., et al., 2017. Zinc oxide nanoparticles: synthesis, antiseptic activity and toxicity mechanism. Adv. Colloid Interface Sci. 249, 37–52. https://doi.org/10.1016/j.cis.2017.07.033.

Lahiri, D., Nag, M., Sheikh, H.I., et al., 2021. Microbiologically-synthesized nanoparticles and their role in silencing the biofilm signaling cascade. Front. Microbiol. 12, 636588. https://doi.org/10.3389/fmicb.2021.636588.

Lazanas, A.C., Prodromidis, M.I., 2023. Electrochemical impedance spectroscopy-a tutorial. ACS Meas. Sci. Au 3 (3), 162–193. https://doi.org/10.1021/acsmeasuresciau.2c00070.

Lazrak, J., El Assiri, E.H., Salim, R., et al., 2025. Exploring the corrosion resistance of mild steel using Cinnamomum cassia extract as a corrosion inhibitor. J. Mol. Struct. 1328, 141401. https://doi.org/10.1016/j.molstruc.2025.141401.

Li, Y., Feng, S., Liu, H., et al., 2020. Bacterial distribution in SRB biofilm affects MIC pitting of carbon steel studied using FIB-SEM. Corros. Sci. 167, 108512. https://doi.org/10.1016/j.corsci.2020.108512.

Li, X., Zhang, L., Wang, Z., et al., 2021. Cellulose controlled zinc oxide nanoparticles with adjustable morphology and their photocatalytic performances. Carbohydr. Polym. 259, 117752. https://doi.org/10.1016/j.carbpol.2021.117752.

Li, C., Wei, B., Cai, Z., et al., 2024. Synthesis and synergistic effects of antibacterial and corrosion inhibition based on concentrated hydrosols of silver nanoparticles. Corros. Sci. 233, 112102. https://doi.org/10.1016/j.corsci.2024.112102.

Liu, H., Fu, C., Gu, T., et al., 2015. Corrosion behavior of carbon steel in the presence of sulfate reducing bacteria and iron oxidizing bacteria cultured in oilfield produced water. Corros. Sci. 100, 484–495. https://doi.org/10.1016/j.corsci.2015.08.023.

Lv, X., Wang, C., Liu, J., et al., 2024. The microbiologically influenced corrosion and protection of pipelines: a detailed review. Materials 17 (20), 4996. https://doi.org/10.3390/ma17204996.

Mahanipour, M.G., Ghaedi, M., 2022. A closer look at SRB souring in porous media: Higher-order finite difference scheme in radial coordinate. J. Petrol. Sci. Eng. 215, 110680. https://doi.org/10.1016/j.petrol.2022.110680.

Moradi, M., Ghiara, G., Spotorno, R., et al., 2022. Understanding biofilm impact on electrochemical impedance spectroscopy analyses in microbial corrosion and microbial corrosion inhibition phenomena. Electrochim. Acta 426, 140803. https://doi.org/10.1016/j.electacta.2022.140803.

Nguyen, T., Roddick, F., Fan, L., 2012. Biofouling of water treatment membranes: a review of the underlying causes, monitoring techniques and control measures. Membranes 2 (4), 804–840. https://doi.org/10.3390/membranes2040804.

Oguzie, E.E., 2008. Evaluation of the inhibitive effect of some plant extracts on the acid corrosion of mild steel. Corros. Sci. 50 (11), 2993–2998. https://doi.org/10.1016/j.corsci.2008.08.004.

Paul, D., Pandey, A., Neogi, S., 2023. Bacterial cell permeability study by metal oxide and mixed metal oxide nanoparticles: analysis of the factors contributing to the antibacterial activity of nanoparticles. World J. Microbiol. Biotechnol. 39 (10), 281. https://doi.org/10.1007/s11274-023-03712-2.

Pereira, G.F., Rosin, T.R., Braga, B., et al., 2024. Evaluation of biofilm inhibition and detachment by commercial biocides in sulfate-reducing bacteria consortia from oil fields. J. Water Process Eng. 63, 105547. https://doi.org/10.1016/j.jwpe.2024.105547.

Ramesh, P., Saravanan, K., Manogar, P., et al., 2021. Green synthesis and characterization of biocompatible zinc oxide nanoparticles and evaluation of its antibacterial potential. Sens. Biosens. Res. 31, 100399. https://doi.org/10.1016/j.sbsr.2021.100399.

Rasheed, P.A., Jabbar, K.A., Rasool, K., et al., 2019. Controlling the biocorrosion of sulfate-reducing bacteria (SRB) on carbon steel using ZnO/chitosan nanocomposite as an eco-friendly biocide. Corros. Sci. 148, 397–406. https://doi.org/10.1016/j.corsci.2018.12.028.

Rashid, M.U., Shah, S.J., Attacha, S., et al., 2024. Green synthesis and characterization of zinc oxide nanoparticles using citrus limetta peels extract and their antibacterial activity against brown and soft rot pathogens and antioxidant potential. Waste Biomass Valoriz. 15 (6), 3351–3366. https://doi.org/10.1007/s12649-023-02389-w.

Rasool, K., Nasrallah, G.K., Younes, N., et al., 2018. "Green" ZnO-interlinked chitosan nanoparticles for the efficient inhibition of sulfate-reducing bacteria in inject seawater. ACS Sustainable Chem. Eng. 6 (3), 3896–3906. https://doi.org/10.1021/acssuschemeng.7b04248.

Rasool, K., Pandey, R.P., Rasheed, P.A., et al., 2021. Screening the growth inhibition mechanism of sulfate reducing bacteria by chitosan/lignosulfonate nanocomposite (CS@LS) in seawater media. J. Environ. Chem. Eng. 9 (6), 106624. https://doi.org/10.1016/j.jece.2021.106624.

Sachin, Jaishree, Singh, N., et al., 2023. Green synthesis of zinc oxide nanoparticles using lychee peel and its application in anti-bacterial properties and CR dye removal from wastewater. Chemosphere 327, 138497. https://doi.org/10.1016/j.chemosphere.2023.138497.

Ščajev, P., Gogova, D., 2024. Long-lived excitons in thermally annealed hydrothermal ZnO. Heliyon 10 (4), e26049. https://doi.org/10.1016/j.heliyon.2024.e26049.

Sharma, S., Kumar, K., Thakur, N., et al., 2020. Ocimum tenuiflorum leaf extract as a green mediator for the synthesis of ZnO nanocapsules inactivating bacterial pathogens. Chem. Pap. 74 (10), 3431–3444. https://doi.org/10.1007/s11696-020-01177-3.

Su, Y., Zhu, M., Zhang, H., et al., 2024. Application of bacterial agent YH for remediation of pyrene-heavy metal co-pollution system: efficiency, mechanism, and microbial response. J. Environ. Manag. 351, 119841. https://doi.org/10.1016/j.jenvman.2023.119841.

Su, Y., Wu, F., Xiao, P., et al., 2025. Facile and green synthesis of Ag/Cu bimetallic nanoparticles using waste banana peel extract for effective corrosion inhibition of mixed sulfate-reducing bacteria. J. Environ. Manag. 373, 123713. https://doi.org/10.1016/j.jenvman.2024.123713.

Tao, L., Guan, C., Wang, Z., et al., 2025. Selenium nanoparticles derived from moringa oleifera lam. Polysaccharides: construction, stability, and *in vitro* antioxidant activity. Foods 14 (6), 918. https://doi.org/10.3390/foods14060918.

Vielkind, M., Kampen, I., Kwade, A., 2013. Zinc oxide nanoparticles in bacterial growth medium: optimized dispersion and growth inhibition of *Pseudomonas putida*. Adv. Nanoparticles 2 (4), 287–293. https://doi.org/10.4236/anp.2013.24039.

Wang, J., Du, M., Shan, X., et al., 2023a. Corrosion inhibition study of marine Streptomyces against sulfate-reducing bacteria in oilfield produced water. Corros. Sci. 223, 111441. https://doi.org/10.1016/j.corsci.2023.111441.

Wang, Z., He, Y., Liu, S., et al., 2023b. Toxic effects of zinc oxide nanoparticles as a food additive in goat mammary epithelial cells. Food Res. Int. 167, 112682. https://doi.org/10.1016/j.foodres.2023.112682.

Wiegand, I., Hilpert, K., Hancock, R.E.W., 2008. Agar and broth dilution methods to determine the minimal inhibitory concentration (MIC) of antimicrobial substances. Nat. Protoc. 3 (2), 163–175. https://doi.org/10.1038/nprot.2007.521.

Wu, F., Feng, Y., Su, Y., et al., 2025. A circular strategy for waste biomass utilization: fruit peel-based ZnO nanoparticles against SRB-induced corrosion. Waste Biomass Valoriz. https://doi.org/10.1007/s12649-025-03383-0.

Xing, G., Tang, Y., Wang, S., et al., 2025. Intelligent antibacterial coatings based on sensitive response and periodic fast drug release for long-term defense against corrosion induced by sulfate-reducing bacteria. J. Colloid Interface Sci. 684, 331–345. https://doi.org/10.1016/j.jcis.2025.01.040.

Yang, X., Shao, J., Liu, Z., et al., 2020. Stress-assisted microbiologically influenced corrosion mechanism of 2205 duplex stainless steel caused by sulfate-reducing bacteria. Corros. Sci. 173, 108746. https://doi.org/10.1016/j.corsci.2020.108746.

Yang, J., Wang, Z.B., Qiao, Y.X., et al., 2022. Synergistic effects of deposits and sulfate reducing bacteria on the corrosion of carbon steel. Corros. Sci. 199, 110210. https://doi.org/10.1016/j.corsci.2022.110210.

Yu, L., Duan, J., Du, X., et al., 2013. Accelerated anaerobic corrosion of electroactive sulfate-reducing bacteria by electrochemical impedance spectroscopy and chronoamperometry. Electrochem. Commun. 26, 101–104. https://doi.org/10.1016/j.elecom.2012.10.022.

Zhao, Q., Li, H., Luo, X., et al., 2025. Research on pulse current cathodic protection technology for long-distance pipeline: a review. Mater. Corros. 76 (1), 20–28. https://doi.org/10.1002/maco.202414557.

Zhu, W., Hu, C., Ren, Y., et al., 2021. Green synthesis of zinc oxide nanoparticles using Cinnamomum Camphora (L.) Presl leaf extracts and its antifungal activity. J. Environ. Chem. Eng. 9 (6), 106659. https://doi.org/10.1016/j.jece.2021.106659.